

Hyperspectral Imager for the Coastal Ocean: instrument description and first images

Robert L. Lucke,¹ Michael Corson,¹ Norman R. McGlothlin,² Steve D. Butcher,²
Daniel L. Wood,² Daniel R. Korwan,¹ Rong R. Li,¹ William A. Snyder,¹
Curt O. Davis,³ and Davidson T. Chen¹

¹Remote Sensing Division, Naval Research Laboratory, 4555 Overlook Avenue,
Washington, District of Columbia 20375, USA

²Praxis, Inc., 5845 Richmond Highway, Suite 700, Alexandria, Virginia 22303, USA

³College of Oceanic and Atmospheric Sciences, Oregon State University, Corvallis, Oregon 97331, USA

*Corresponding author: robert.lucke@nrl.navy.mil

Received 29 July 2010; revised 16 November 2010; accepted 17 January 2011;
posted 7 February 2011 (Doc. ID 132361); published 1 April 2011

The Hyperspectral Imager for the Coastal Ocean (HICO) is the first spaceborne hyperspectral sensor designed specifically for the coastal ocean and estuarial, riverine, or other shallow-water areas. The HICO generates hyperspectral images, primarily over the 400–900 nm spectral range, with a ground sample distance of ≈ 90 m (at nadir) and a high signal-to-noise ratio. The HICO is now operating on the International Space Station (ISS). Its cross-track and along-track fields of view are 42 km (at nadir) and 192 km, respectively, for a total scene area of 8000 km². The HICO is an innovative prototype sensor that builds on extensive experience with airborne sensors and makes extensive use of commercial off-the-shelf components to build a space sensor at a small fraction of the usual cost and time. Here we describe the instrument's design and characterization and present early images from the ISS. © 2011 Optical Society of America

OCIS codes: 010.0280, 280.4788, 280.1355.

1. Introduction

The Hyperspectral Imager for the Coastal Ocean (HICO) sensor is the first spaceborne hyperspectral imager designed specifically for the coastal environment. The HICO builds on the legacy of the Naval Research Laboratory (NRL)'s airborne hyperspectral remote sensing program. Extensive experience developing and operating the PHILLS airborne hyperspectral imagers [1,2] enabled NRL's Remote Sensing Division to begin with a set of requirements for HICO in May 2007 and deliver a space-qualified instrument for integration and spacecraft-level testing in September 2008. The HICO is intended to be a pathfinder for follow-on sensors with better spatial,

and perhaps spectral, resolution designed for routine observations of littoral, riverine, and estuarine environments.

Visible and near-infrared (near-IR) wavelengths in the range of 400 to 700 nm constitute the only portion of the electromagnetic spectrum that significantly penetrates water and directly probes the water column. But the fraction of light that is returned from below the surface is small, typically less than 20% of the total signal, with the rest being from reflections on the sea surface and from the intervening atmosphere. The combination of a low signal over a narrow spectral range and large contamination of that signal by atmospheric scattering dictates very stringent requirements for maritime hyperspectral imaging that are usually not met by systems designed for land applications [3].

Retrieval of environmentally relevant quantities requires a signal-to-noise ratio (SNR) of about 200 or better for water-penetrating wavelengths, recorded in contiguous spectral bands of about 5–10 nm width [3] to resolve the spectral features in the scene. In addition, spectral image data from 700 to 900 nm are used to account for light from surface reflections and the effects of the atmosphere, so that light returned from below the surface can be measured and analyzed. The HICO produces its best data over the 400–900 nm spectral range. The spectral sampling interval is 5.7 nm.

In the complicated coastal environment, where the water contains significant dissolved and suspended matter and the bottom may be detectable, analysis of hyperspectral imagery has demonstrated the ability to retrieve bathymetry, bottom type, chlorophyll content, and the inherent optical properties of the water [2,4]. To capture the scale of coastal dynamics, areal coverage of thousands of square kilometers is desirable. A typical HICO image covers more than 8000 sq km with a ground sample distance (GSD) of approximately 90 m.

The HICO sensor, shown in Fig. 1, is part of the HICO-RAIDS experiment payload (HREP). The Re-

mote Atmospheric and Ionospheric Detection System (RAIDS) instruments have been described elsewhere [5–7]. The HREP is a rectangular box 1.82 m long by 0.8 m wide by 0.8 m high, having a total mass of 381 kg, with HICO mounted inside the box. The HICO sensor's envelope, including the mounting and pointing system, is 0.89 m long by 0.53 m wide by 0.43 m high, and its total mass is 41 kg.

The HREP was launched from the Tanegashima Space Center on 11 September 2009 on a Japanese HII-B rocket and transferred to its operating location on the Japanese Experiment Module–Exposed Facility on the International Space Station (ISS) on 24 September 2009. Check out of the HICO sensor was completed in a few days, and it has been fully functional since 1 October 2009. The HREP was built for a mission duration of one to three years, after which it will be removed from the ISS and deorbited.

When the ISS is in its normal flight mode, the HREP's long axis is parallel to the velocity vector, as is the HICO's rotation axis (see Fig. 1). The HICO is mounted inside the box, completely enclosed by the HREP, except for a viewing slot in the bottom of the box through which it views the Earth. A facsimile of this slot is shown in Fig. 1. As explained in more

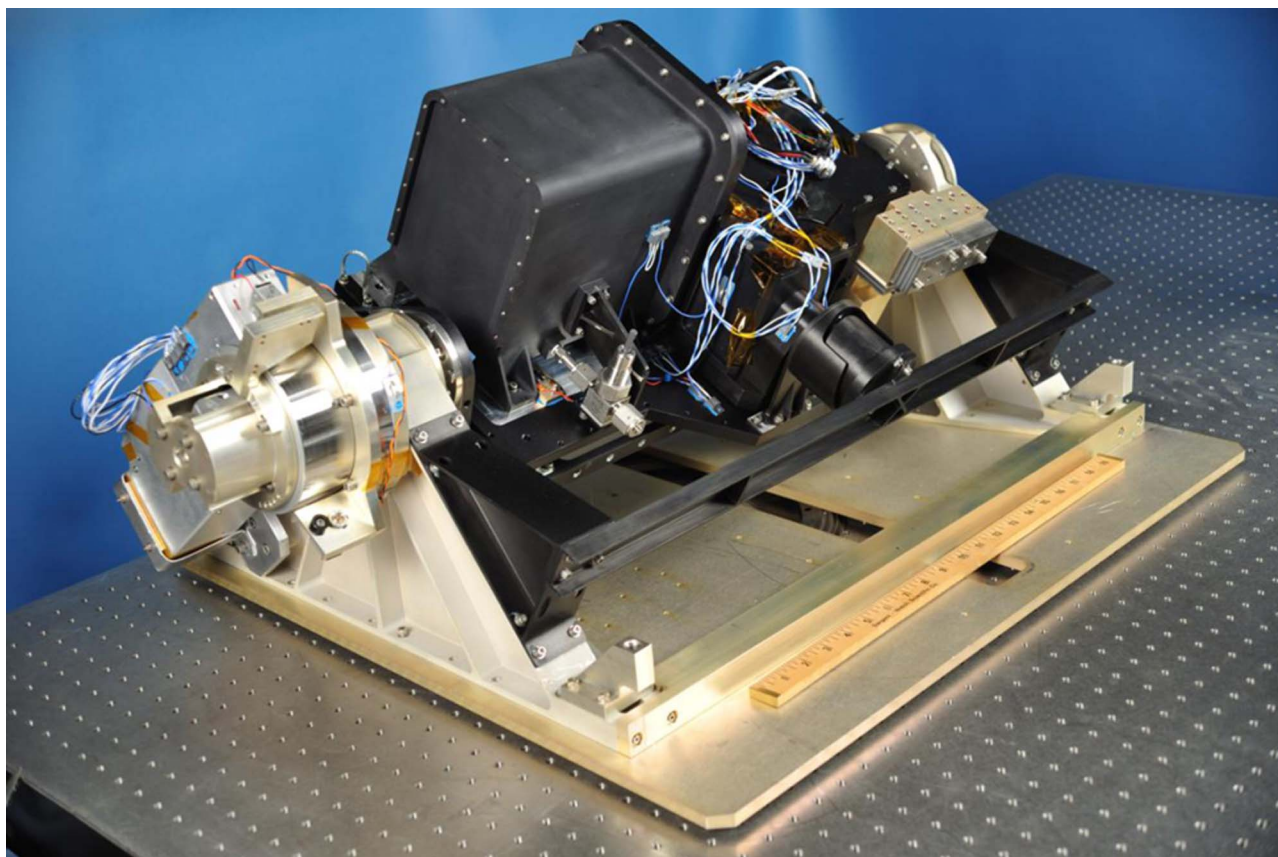


Fig. 1. (Color online) The HICO shown before installation of thermal blankets and integration into the HREP. The Newport rotator is on the left. The high black box at the center is hermetically sealed and contains the Rolera-MGi camera. The shorter black box just beyond the camera housing is the spectrometer, to which the lens, just to the right of the center, is attached. The sensor is in stow position, with the lens looking into a labyrinth light seal, which is supported on the black longitudinal cross bar. The sensor is bolted to its nonflight mounting plate, which reproduces the slot through which it will view the Earth. The ruler is marked in inches. The normal flight direction is from right to left, parallel to the rotation axis.

Table 1. HICO Parameters

| | Value | Comment |
|--|--|--|
| ISS | | |
| Orbital altitude | ≈350 km | May rise to 400 km over a 1–3 year mission |
| Inclination | 51.6° | HICO's latitude range ≈ + 54° / – 53°; it covers 80% of the Earth's surface |
| Period | 91.5 min | 15.7 orbits/day; the HICO can do one scene per orbit |
| Ground speed | 7.0 km/s | Speed of sub-ISS point on ground, includes Earth rotation |
| HICO Hardware Lens | | |
| FL | 67.16 mm | Gives 83 m nadir IFOV for 16 μm pixels and 350 km altitude |
| Clear aperture | 19 mm | <i>f</i> /3.5 gives desired radiometrics |
| FOV | 6.92° (±3.46°) | Covers 512 cross-track pixels (see Subsection 2.C) |
| Spectrometer | | |
| Slit width | 16 μm | Matches CCD pixel size |
| Blaze wavelength of grating | 400 nm | High efficiency in first-order blue light |
| Blazed fraction of groove | ≈90% of groove spacing | High efficiency |
| CCD | | |
| Pixel size | 16 μm | CCD97 from e2v Technologies Gives 83 m nadir IFOV for 16 μm pixels and 350 km altitude |
| IFOV | 0.01365° | See Eq. (2) |
| Array size, total used | 512 × 512 512 (spatial) × 384 (spectral) | One spatial pixel = 83 m at 350 km altitude; one spectral pixel = 1.91 nm |
| Spectral sample width (normal) | 5.73 nm | Three-pixel on-chip binning |
| Spectral sample width (HR mode) | 1.91 nm | On-orbit wavelength calibration check (no binning) |
| Digitization | 14 bits | Maximum DN = 16,383 |
| Dark noise | ≈3.8 DN | Dynamic range: 16,000/3.8 = 4200 |
| Photoelectrons/DN | 26 ± 2 | Photon-limited SNR = $\sqrt{26 \times \text{DN}}$ |
| Operations | | |
| Stable exposure time | 12.64 ms (28.94 ms in HR mode) | See Subsection 2.A and Appendix A |
| Frame transfer time | 1.11 ms | See Subsection 2.A and Appendix A |
| Exposure time (total frame time) | 13.75 ms (12.64 + 1.11) (30.05 ms in HR mode) | Along-track GSD = 96 m (210 m in HR mode) |
| Scene time | 275 s (0.01375 × 2000) 15 s (0.03 × 500) in HR mode | Scene = 2000 frames in normal mode and 500 frames in HR mode |
| Data volume normal mode | | |
| Data bytes/frame | 512 × 128 × 2 = 131 KB | BIL format |
| Frames per observation | 200 dark + 2000 scene + dark = 2400 total | (13.75 ms/frame) × (2000 frames) ⇒ 2.75 s to record scene |
| Data bytes/scene | 131 KB × 2400 = 315 MB | — |
| Data volume HR (hi-res.) mode | | |
| Data bytes/frame | 512 × 384 × 2 = 393 KB | BIL format |
| Frames per observation | 100 dark + 500 scene + 100 dark = 700 | (30.05 ms/frame) × (500 frames) ⇒ 15 s to record scene |
| Data bytes/scene | 393 KB × 700 = 275 MB | — |
| Performance | | |
| Off-nadir pointing (normal flight mode) | 45° to port (north), 30° to starboard (south) | Accessible ground swath ≈550 km |
| Observed ground swath width | 42 km (nadir, 350 km altitude) | Up to 92 km at 45° off nadir |
| GSD | 83 m cross-track (nadir, 350 km altitude) | Proportional to altitude |
| GSD | 96 m along track (210 m in HR mode) | Proportional to frame time |
| Scene length | 192 km (2000 × 96 m) (105 km in HR mode) | Maximum, can be shorter |
| Scene area | (42 km wide) × (192 km long) ≈8000 km ² (nadir view) | Encompasses the scale of coastal dynamics |
| Spectral range | Nominal: 350–1080 nm; best data: 400–900 nm | — |
| Spatial FWHM | 1.6 pixels typical (130 m at nadir, 350 km) | See Fig. 3 |
| Spectral FWHM | 1.9 pixels typical (3.6 nm) | See Fig. 5 |
| Keystone | <0.2 pixels (0.4 nm), mostly | Minimal spatial smearing; see Fig. 4 |
| Spectral tilt | <0.15 pixels (0.3 nm), mostly | Minimal spectral smearing; see Fig. 6 |
| Spectral smile | Negligible | See Fig. 6 |
| Polarization sensitivity | <4% for most wavelengths | See Fig. 7 |
| SNR | >200:1 over 400–600 nm for shallow water (see Fig. 13) | For 11.46 nm spectral bins, allows removal of atmospheric effects |

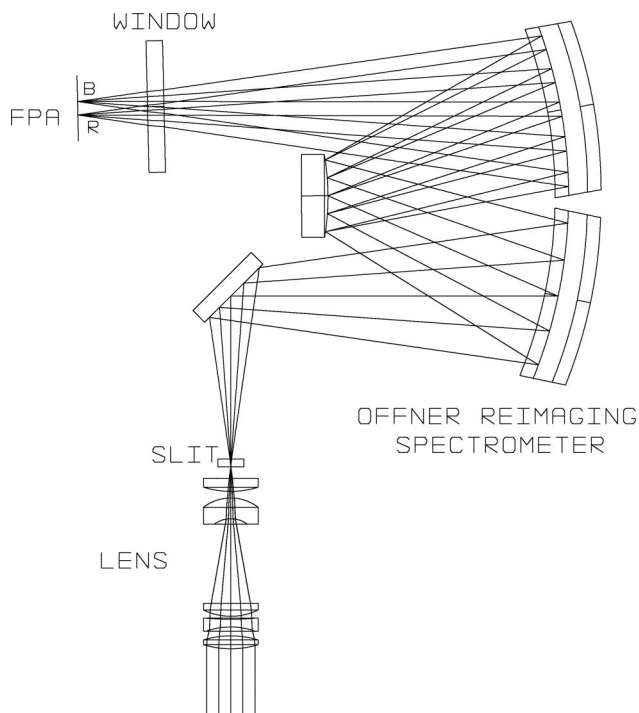


Fig. 2. Optical configuration of the HICO instrument. The grating is ruled on the convex Offner secondary and spreads the image of the slit over blue to red wavelengths in the focal plane. The long axis of the slit is perpendicular to the page. The window between the spectrometer and the camera keeps the N_2 gas sealed in the camera housing.

detail in Section 3, a scene is selected by rotating HICO's line of sight (LOS) to a location along this slot; the orbital motion of the ISS then scans the LOS along the scene in pushbroom fashion.

The altitude of the ISS is currently about 350 km, and the inclination of its orbit is 51.6° , which means that it is possible to image about 80% of the Earth's surface, including all tropical and most temperate coastal regions, with the HICO. The orbital period is 91.5 min (15.7 orbits/day), and the HICO can record one scene per orbit. A scene is typically $42 \text{ km} \times 192 \text{ km}$ or 8000 sq km.

Some preliminary reports on the HICO sensor and its data have been given elsewhere [8–11]; in this paper we give a detailed description of the sensor. The parameters of the sensor and of its observations are listed in Table 1. Section 2 covers the intrinsic properties of the instrument; Section 3 describes the GSD, size, and orientation of the HICO's ground footprint; Section 4 describes how observation are made; and Section 5 gives some early experience with the instrument.

2. Instrument Characteristics

A. General

The HICO is a conventional hyperspectral imaging sensor, incorporating an Offner grating-type spectrometer [12] and covering a scene in pushbroom mode. The optical layout is shown in Fig. 2. The lens, spec-

trometer, and camera are mounted on a rigid optical bench that is attached by silicon-rubber isolators to a cradle that is rotated about a horizontal axis to direct the LOS to the desired off-nadir direction (see Fig. 1). Rotation is effected by a vacuum-rated Newport rotator, model number RV120PEV6. The lens views the Earth through a slot in the bottom of the HREP housing. The lens is mounted on the spectrometer, and both operate in vacuum. The camera is a commercial off-the-shelf laboratory unit, not built to operate in vacuum, and it is therefore housed in a sealed container. A fused silica window admits light from the spectrometer. The spectrometer and camera housing are bolted to the optical bench but not to each other.

The camera is a Photometrics QImaging Rolera-MGi, incorporating a 512×512 CCD with $16 \mu\text{m}$ pixels. The electron-multiplying feature is not used. Modifications for spaceflight consisted primarily of conformally coating the PC boards and adding stiffening to their mountings. The only other modification was to deactivate the thermoelectric cooler and remove most of the copper cooling fins that dissipate heat from the cooler (the latter was done to reduce launch strains on the camera's mounting screws). The cooler was deactivated because it consumes about 80 W of power, and, in the HICO's mounting configuration on the spacecraft, we could not dissipate that much heat. Consequently, the temperature of the CCD detector is not held constant, and the dark counts change as the temperature changes. Thus, if the CCD's initial temperature changes from one scene to the next, the dark counts also change. More troublesome, the CCD warms up and cools down during an observation, which makes the dark count rate a function of time during the collection of data. The computer processing done to subtract the dark counts from the measured data is described in Appendix A.

The Rolera camera uses the CCD97 focal plane array from e2v Technologies. This is a thinned, back-side-illuminated frame-transfer CCD with a 512×512 exposed frame to record light and a 512×512 covered storage frame into which charge packets from the exposed frame are rapidly transferred for subsequent (slower) readout. The bulk of the light is recorded during the stable exposure time, T_1 , which is normally 12.64 ms. During the transfer time, $T_2 = 1.11$ ms, the exposed frame is clocked "vertically" (the spectral direction), one row at a time, into the storage frame. The problem is that during the transfer time, charge packets accumulate more charge from the light that falls on the pixels through which they pass, for a total exposure time of $T_1 + T_2 = 13.75$ ms. This effect must be accounted for to achieve high radiometric accuracy, because the non-negligible fraction $T_2/(T_1 + T_2) = 1.11/13.75 = 8\%$ of the charge that one wishes were in a pixel is actually smeared out over all pixels in that column. The data processing done to correct for this effect is described in Appendix B.

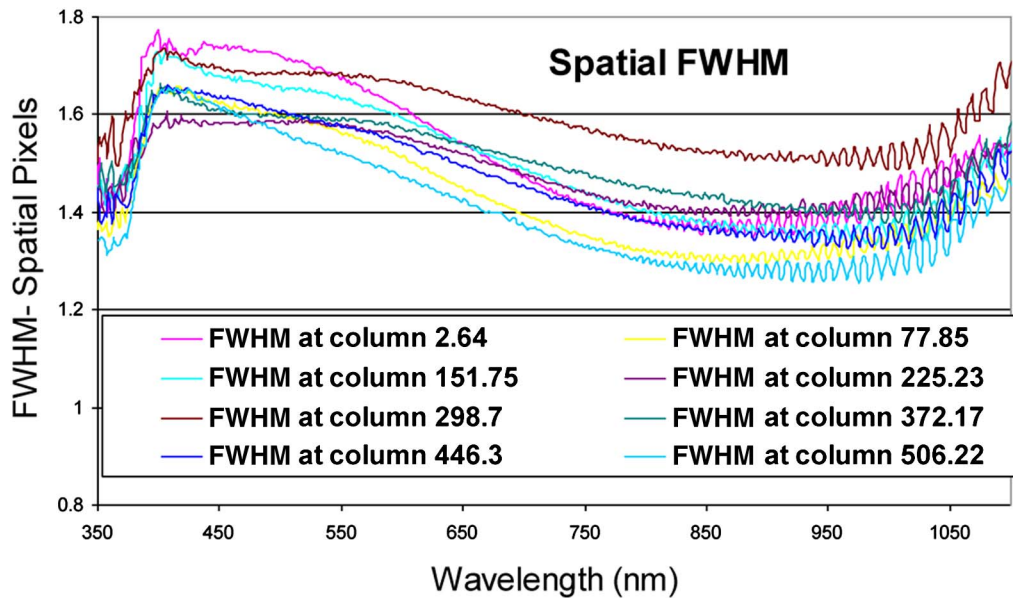


Fig. 3. (Color online) FWHM of the PSF in the spatial direction. Below about 390 nm, the light source was too weak to give reliable results. The oscillations at the long-wavelength end of the curves is caused by etaloning within the thinned, back-illuminated CCD.

The spectrometer is a standard unit from Brandywine Photonics, Inc., of Chester, Pennsylvania, slightly modified for spaceflight by the use of vacuum-compatible epoxies and fasteners. This instrument was chosen for its high grating efficiency, estimated at $\approx 80\%$ at the blaze wavelength (400 nm). The lens, also supplied by Brandywine, was custom-built for the HICO. The spectrometer's slit width is $16\ \mu\text{m}$. It is reimaged at 1:1 magnification onto the $16\ \mu\text{m}$ pixels of the CCD.

The CCD's 512 spectral pixels cover a nominal wavelength range of 350–1325 nm. The region of interest (ROI) is normally set to the first 384 pixels, covering 350–1080 nm, which include the primary ROI for maritime hyperspectral remote sensing: the 400–900 nm spectral range. The CCD's other 128 spectral pixels are discarded, primarily because the frame time of 13.75 ms could not be achieved if they were recorded, but also because they do not contain valid spectral information. Because silicon does not respond to light beyond about 1100 nm, the response in most of this region is from light acquired during frame transfer. Shorter wavelength light from higher orders of diffraction from the grating also contributes.

Because HICO's nominal spectral range of 350–1080 nm covers more than a factor of 2 in wavelength, it follows that second-order light from the wavelengths 350–540 nm falls in the same pixels as first-order light from 700–1080 nm. This effect was measured in the laboratory, but it has proved more efficacious to correct for second-order light on the basis of orbital data. We can do this with the HICO because the shorter wavelengths, e.g., 400 nm, penetrate the water, while the “times-two” wavelengths, e.g., 800 nm, do not. Consequently, second-order light at 400 nm causes underwater structures to appear in 800 nm images. These artifacts can be

used to measure the fraction of the shorter wavelength light that falls in the longer wavelength band. This fraction is then used to correct the data from all scenes [13]. Second-order light from shorter wavelengths can in principle cause an uncorrectable error because it is not measured in the first order, but this effect is expected to be unimportant, partly because there is relatively little light at these wavelengths in natural scenes, but mostly because the instrument's sensitivity is quite low below 350 nm. The transmission of the lens (due to the glass composition of its elements) is not more than about 10%, and the quantum efficiency of the CCD is not more than 20%.

Scattered light levels are low in the HICO sensor. An analysis of scattered light will be the subject of a future publication.

The HICO has two modes of operation. Spreading $1080 - 350 = 730\ \text{nm}$ of spectrum over 384 pixels means that each pixel covers $1.91\ \text{nm}$ (see Subsection 2.D). In normal mode, pixels 1 to 384 are binned by three at readout to yield 128 bins covering $5.73\ \text{nm}$ per bin. Thus, one complete frame of data contains $512 \times 128 = 65,536$ data samples. Each sample is digitized to 14 bits and read out as a 16 bit word. The camera also has a high-resolution (HR) mode of operation in which pixels are not binned at readout, so the $1.91\ \text{nm}$ spectral sampling is preserved. In HR mode, a frame of data contains $512 \times 384 = 196,608$ data samples. This mode will be used on occasion to check the sensor's spectral calibration. It is used only occasionally because the frame time is more than twice as long as in normal mode (see Table 1), with a concomitant increase in the along-track GSD.

B. Optical Performance

As indicated in Fig. 2, the spectrometer forms spectrally dispersed images of the slit on the CCD. It is

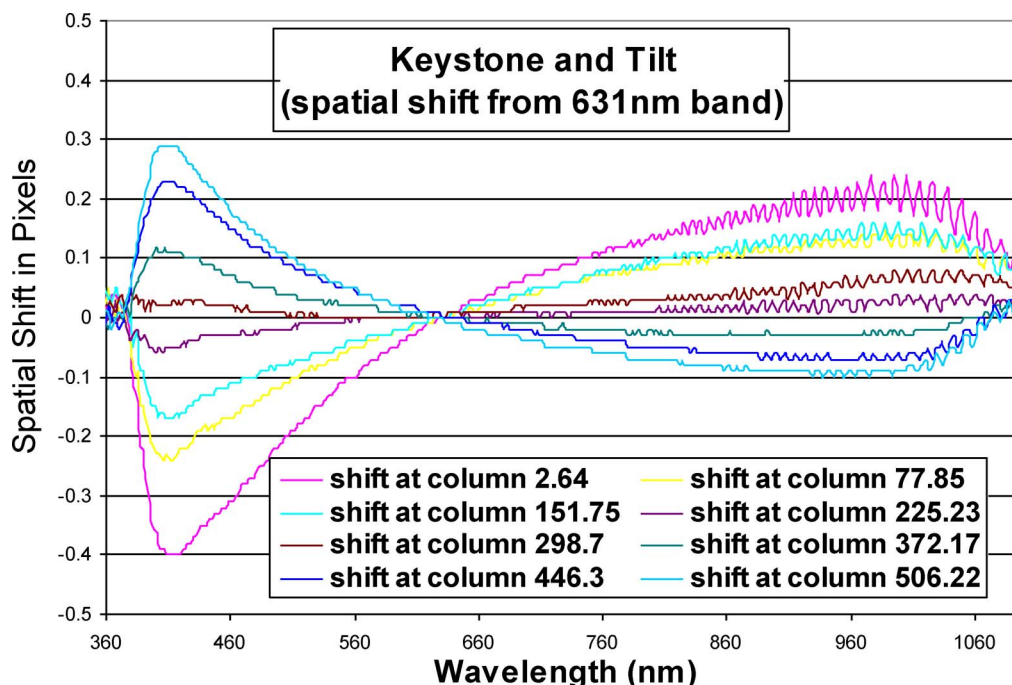


Fig. 4. (Color online) Keystone and tilt. The deviations from a straight horizontal line at zero shift are due primarily to residual chromatic aberrations in the lens. Below about 390 nm, the light source was too weak to give reliable results.

highly desirable that these images, in addition to being sharply focused, be straight, not curved, at all wavelengths, i.e., not subject to spectral “smile.” The CCD can then be adjusted so that these images are accurately parallel with the rows of pixels. Similarly,

the spectra of points in the scene should be accurately parallel to the columns of pixels, that is, not exhibit significant tilt or distortions of the type that are lumped under the term “keystone.” An advantage of the Offner spectrometer for hyperspectral imaging

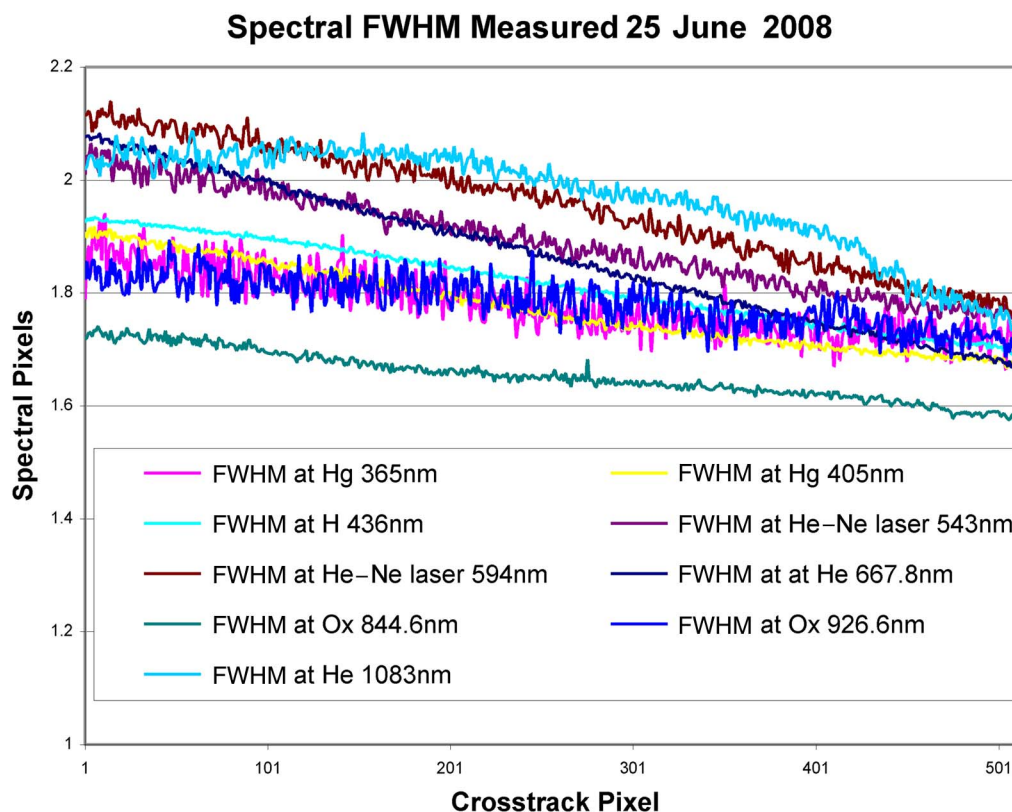


Fig. 5. (Color online) FWHM of the PSF in the spectral direction.

Tilt (& Smile) Measured 25 June 2008
(spectral shift in pixels from spatial pixel 256 = array center)

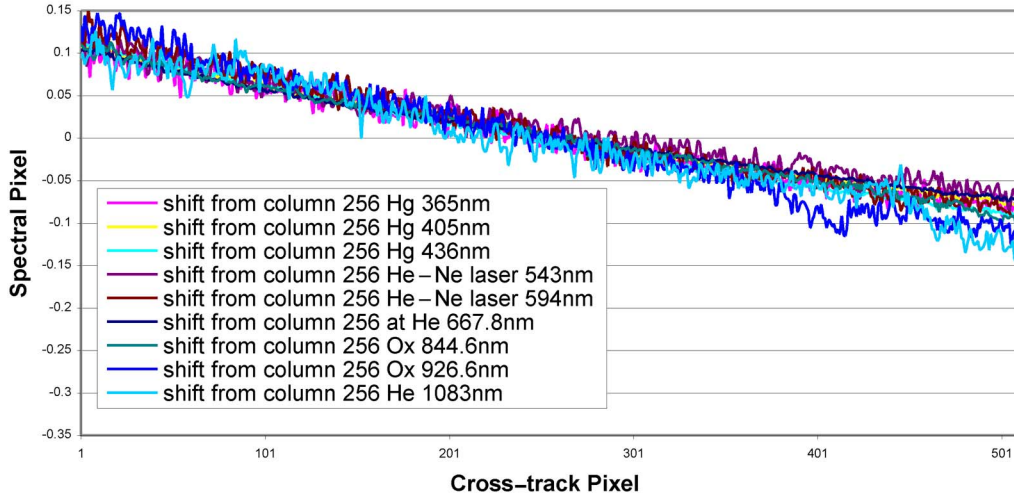


Fig. 6. (Color online) Spectral tilt and (nearly nonexistent) smile.

is that, when properly aligned, it images the slit with very low distortion at all wavelengths, thereby minimizing smile and keystone. Keystone-type distortion is then limited by lateral color in the lens, that is, by the fact that the focal length (FL) of the lens has a slight wavelength dependence. Once the spectrometer has been aligned, the CCD is carefully positioned so that its face lies accurately in the spectrometer's focal plane; i.e., it is sharply focused, and rotated so that its rows and columns match the along-slit and dispersion directions of the image.

The optical data required to characterize focus and keystone in the spatial direction were obtained by mounting the sensor in front of a collimator (an off-axis paraboloid) on a precision rotation stage. The stage was rotated so that the image of the source moved along the slit, that is, in the spatial direction, through 6.8° in seven steps of 1° and one step of 0.8° , to cover the sensor's 6.9° field of view (FOV). At each input angle, the sensor formed a spatial point spread function (PSF), spectrally dispersed. Gaussian curves were fit to the digital number (DN) values of the several spatial pixels that showed a significant response, and the full-width at half-maximum (FWHM) of these fits is shown in Fig. 3. Similarly, Fig. 4 shows the shift in the centroids of these fits, that is, it shows tilt and keystone across the array. Below about 390 nm, the light source was too weak to give reliable results. The overall tilt in Fig. 4 can be seen to be about 0.15 pixels over the 384 pixels covering the 350–1080 nm spectral range.

Focus, tilt, and spectral smile were obtained by illuminating the slit with diffuse monochromatic light from standard laboratory sources (lasers and low-pressure spectral calibration lamps) and fitting a Gaussian to the several spectral pixels that showed a significant response. Figure 5 shows the FWHM of the spectral PSF, and Fig. 6 shows the centroid shifts.

The as-built optical system has a small amount of astigmatism in it. Because spatial pixels are not binned, while spectral pixels are normally binned by three, the focus was adjusted (by positioning the CCD) so that the image is sharpest in the spatial direction. Figure 3 shows that the FWHMs of the PSF in the spatial direction are typically about 1.6 pixels, which, based on our experience with the PHILLS program [1], we consider to be very good performance for a hyperspectral sensor. Figure 5 shows FWHMs that are a little larger in the spectral direction.

The FWHM in Fig. 3 is a reasonable measure of the sensor's spatial resolution (as opposed to its GSD, which is discussed in Section 3). The spectral FWHM in Fig. 5 is taken in HR mode with no binning at readout. Taking 1.9 pixels as a representative value gives a spectral resolution of $1.9 \times (1.91 \text{ nm}) \approx 3.6 \text{ nm}$. Normally, spectral pixels are binned by three at readout, and the spectral sampling is then $3 \times (1.91 \text{ nm}) = 5.73 \text{ nm}$.

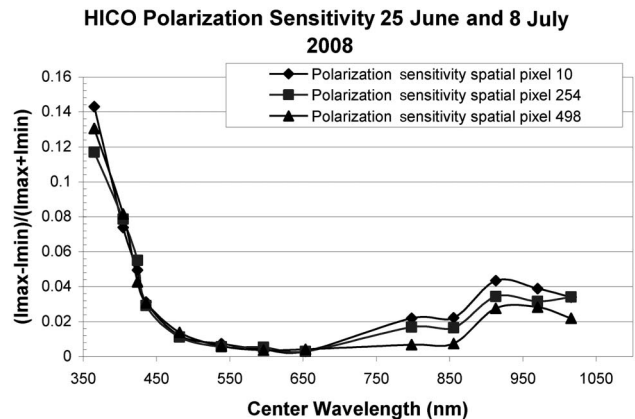


Fig. 7. Polarization sensitivity of the HICO. The sensor is most sensitive to blue light polarized parallel to the slit and to red light polarized perpendicular to the slit.

Figure 4 shows that keystone is below 0.2–0.3 pixels nearly everywhere when 630 nm is chosen as the reference wavelength. This results in a minimal mixing of the spectrum of one spatial pixel with its neighbor. Spectral tilt is shown in Fig. 6 to be no more than about 0.2 pixels or $0.2 \times 1.91 \approx 0.4$ nm across the 512-element array, commensurate with the 0.15 pixels across 384 elements in the spatial tilt shown in Fig. 4. The smile (curvature) in Fig. 6 causes a slight deviation from a straight-line fit, approximately ± 0.01 spectral pixels.

Figures 3–6 show that the HICO's optical alignment is very good. Ideally, the curves in Figs. 3 and 5 should be identical horizontal lines. We attribute the tilt part of the deviations from this ideal to imperfect alignment between the columns of the CCD and the slit of the spectrometer, and we attribute the remainder to imperfect alignment of the mirrors in the Offner spectrometer. The regular oscillations in the right-hand side of Fig. 3 are real, caused by "etaloning," that is, by the fact that the longer wavelengths are becoming comparable to the size of vertical structures in the CCD detector (the same is true of Fig. 4).

Laboratory investigation showed no vignetting anywhere in the optical system and no measurable variations in the width of the slit, which is a laser-etched device and therefore expected to be very uniform.

Polarization sensitivity was measured with three different polarizers, one each for the UV ($\lambda < 450$ nm), Vis ($450 < \lambda < 700$ nm), and near-IR ($700 < \lambda$) regions. Figure 7 shows the sensor's polarization sensitivity as a function of wavelength for three spatial pixels: at the center and edges of the CCD. The HICO is most sensitive to light with the polarization direction parallel to the slit. Polarization sensitivity is quite low ($< 5\%$) except at the bluest wavelengths. If necessary, we will make a correction in data processing similar to what is done for the MODIS sensor for ocean scenes [14,15].

C. Angular Field of View and IFOV

The data from which Fig. 4 was obtained were also processed to relate field angle, given by the rotation angle of the rotation stage, to image location in the focal plane, given by the centroid of the PSF. The best fit to these data at $\lambda = 630$ nm is

$$\theta(p) = 3.487 \frac{p - 256.5}{255.5} - 0.035 \left(\frac{p - 256.5}{255.5} \right)^3 \text{ deg}, \quad 1 \leq p \leq 512, \quad (1)$$

where θ is the angle between the LOS of the center point of the array and the LOS of the center of pixel p . In Eq. (1), p describes an exact location along the spatial dimension of the CCD. When p is a whole number, it describes the center of a pixel. The center of the array is located between pixels 256 and 257, at $p = 256.5$. The centers of pixels 1 and 512 are located

255.5 pixels away from this center. The sign convention chosen for Eq. (1) puts the LOS of pixel 1, which views the port (north) side of the ground scene, at -3.452° from the center of the FOV when the ISS is in normal flight orientation. Pixel 512, at 3.452° , views the starboard (south) side of the ground scene. Thus, as θ increases in a positive sense, the observed point on the ground moves in the starboard direction.

The cubic term in Eq. (1) describes Seidel distortion. Distortion is zero along the optic axis of the lens, so Eq. (1) says that the optic axis of the lens is aligned with the center of the array. While this cannot be exactly true, it is true to the precision of our measurement, which we estimate has an error of about ± 2 pixels.

The data in Fig. 4 can be used to adjust Eq. (1) for other wavelengths as needed. A positive pixel shift means that, with respect to 631 nm, the same field angle falls at a (slightly) larger pixel number. Thus, in order to write Eq. (1) for a different wavelength, it is necessary only to replace p by $p - \delta p$, where δp is the pixel shift from Fig. 3. The width of a pixel is $\Delta p = 1$ and the instantaneous FOV (IFOV) of a pixel is

$$\begin{aligned} \text{IFOV} &= \frac{d\theta(p)}{dp} \Delta p = \frac{3.487}{255.5} - \frac{0.105}{255.5} \left(\frac{p - 256.5}{255.5} \right)^2 \\ &= 0.01365 - 0.00041 \left(\frac{p - 256.5}{255.5} \right)^2 \text{ deg}. \end{aligned} \quad (2)$$

Equation (2) says that the IFOV is 3% smaller at the edge of the CCD than at the center. The maximum distortion of 0.035° from Eq. (1) is about 2.5 pixels. The (Gaussian) FL is given by the pixel size at the center of the CCD divided by the tangent of the IFOV:

$$\text{FL} = \frac{0.016 \text{ mm}}{\tan(0.01365^\circ)} = 67.16 \text{ mm}. \quad (3)$$

The edges of the array are at $p = 0.5$ and $p = 512.5$, so, from Eq. (1), the angular FOV is $\theta(512.5) - \theta(0.5) = 6.92^\circ$.

Table 2. Wavelengths of Laboratory Calibration Spectral Lines and Pixel Numbers

| λ (nm) | Pixel No. |
|----------------|-----------|
| 365.9 | 9.34 |
| 389.8 | 21.39 |
| 405.6 | 30.01 |
| 436.7 | 46.32 |
| 487.0 | 71.67 |
| 544.4 | 102.68 |
| 588.5 | 125.59 |
| 594.9 | 129.21 |
| 657.2 | 160.85 |
| 668.7 | 167.66 |
| 707.4 | 187.92 |
| 845.5 | 259.63 |
| 927.5 | 302.45 |
| 1047.9 | 366.76 |
| 1083.9 | 385.31 |

D. Wavelength Calibration

Wavelength calibration was measured in the laboratory using diffuse monochromatic light from standard laboratory sources (lasers and low-pressure spectral calibration lamps) and fitting a Gaussian to the spectral pixels that showed a significant response. Table 2 shows the HICO calibration wavelengths and the spectral pixel numbers of their image centroids on the CCD, for a spatial pixel near the center of the array (No. 252). A linear least-squares fit to these data with a root-mean-square (rms) error of 0.79 nm is

$$\lambda_c = 348.8 + 1.9095p \quad 1 \leq p \leq 384, \quad (4)$$

where λ_c is the wavelength in nanometers at the center of pixel p . Figure 6 exhibits spectral tilt and shows that variation in the wavelength calibration across the spatial dimension of the array is quite small, never exceeding 0.15 pixels or 0.3 nm.

Analysis has shown that using higher powers of p in Eq. (4) is not justified because it does not substantially reduce the rms error of the fit. This comports with optical spot centroids calculated with ZEMAX [16], which show that the as-designed system has an extremely linear relation between wavelength and image location in the focal plane.

Equation (4) is expressed in terms of pixels and is the expression to use in HR mode. In normal mode, pixels are binned by three at readout, so Eq. (4) becomes

$$\lambda_c = 346.9 + 5.728b \quad 1 \leq b \leq 128, \quad (5)$$

where λ_c is now the wavelength at the center of spectral bin b .

On-orbit wavelength calibration has shown a uniform difference from the laboratory calibration. The wavelength calibration changed by 1.7 nm immediately after launch then settled in at 0.9 nm as of June 2010. It has not changed since then. This difference is discussed briefly in Section 5. As a result of this on-orbit calibration, 0.9 nm has been added to all laboratory wavelengths, that is, to all wavelengths in Eqs. (4) and (5) and Table 2. The waveband per pixel and the rms errors in Eqs. (4) and (5) are unaffected. Wavelength calibration will be monitored using Fraunhofer lines and atmospheric absorptions lines to see if it changes in the future.

E. Radiometric Calibration

As part of the calibration procedure, it was established that one DN from the analog-to-digital (ADC) converter corresponds to approximately 26 detected photoelectrons. The photon shot noise, expressed in counts, is therefore given by $[(\text{signal DN})/26]^{1/2}$, e.g., for a signal of 1000 DN, the shot noise is 6.3 DN. The random dark noise of the CCD is typically about 3.8 counts, so we can say that as long as the DN value in a spectral bin is about 400 or greater, the sensor is essentially photon-noise-limited. The ADC converter

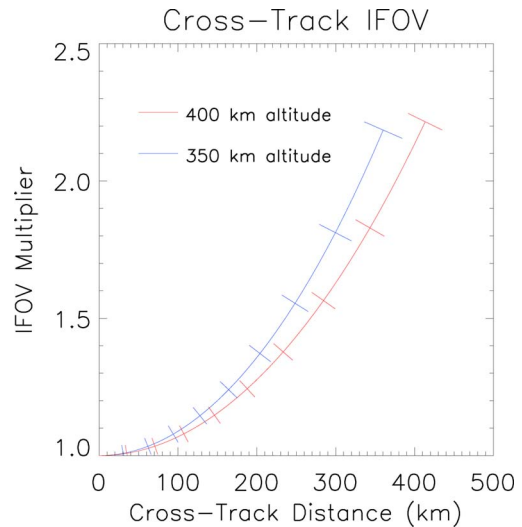


Fig. 8. (Color online) Cross-track IFOV (and FOV; see text) ground-footprint size multiplier as a function of the off-track distance of the observed ground point for altitudes that will cover the range of ISS altitudes for the HREP mission. Tick marks are placed on the curves every 5° of the off-nadir pointing angle. The HICO can achieve off-nadir angles of 45° to starboard and 30° to port.

performs 14 bit digitization, so the maximum signal is 16,383 DN. An offset of 200–350 DN (the exact number depends on pixel and temperature) is imposed to assure that no signals go “below zero.” The dynamic range of the sensor is 16000/3.8 = 4200.

The radiometric calibration carried out in the laboratory on the HICO sensor will not be described in detail here because data from orbit indicate that, somewhere between the laboratory and the ISS, the HICO lost about 25% of its sensitivity. The reason for this is unknown. This issue is being addressed with vicarious calibration (see Section 6), and the HICO’s radiometric calibration will be the subject of a future publication.

3. Ground Coverage, Ground Sample Distance, and Scene Orientation

The inclination of the ISS orbit is 51.6° [17]. The HICO’s LOS can be directed from approximately 45° to port (north) of the ground track to approximately 30° to starboard (south). The corresponding ground-point distances from the satellite’s ground track are approximately 350 and 200 km or about 3° and 2° of latitude, respectively. Thus the HICO has access to about 80% of the Earth’s surface. Cross-track ground coverage is provided by the sensor’s 6.92° FOV and along-track coverage by the motion of the ISS.

The orbital altitude of the ISS is variable. At this time, it is about 350 km, but it may rise as high as 400 km by the end of the HREP mission [18]. As given in Table 1, the 16 μm pixel size of the CCD and the 67.16 mm FL of the lens combine to yield a cross-track IFOV, which is the same as the cross-track GSD, of 83 m for a nadir view from 350 km, reasonably well suited to the scale of coastal features [3].

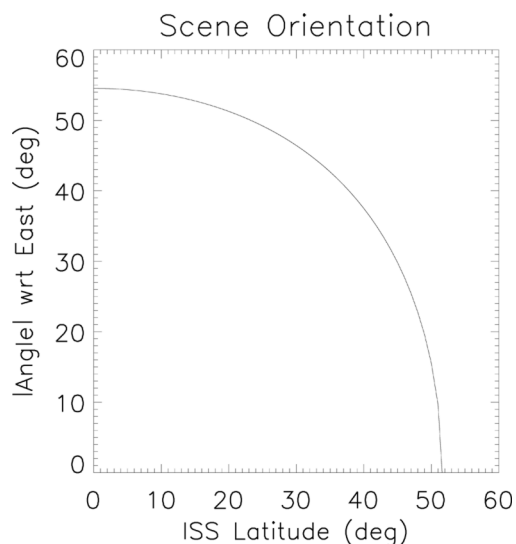


Fig. 9. The absolute value of the angle that the long axis of a HICO scene makes with respect to due east. The angle is positive when the ISS is moving north and negative when it is moving south. The value of the angle is exact for a nadir view and errs by at most (depending on latitude) about 1.6° for the extreme case of a 45° off-nadir observation.

Figure 8 shows the factor by which the HICO's cross-track IFOV changes with off-nadir angle. The same factor can be applied to the width of the observed ground swath, which is determined by the 6.92° FOV. These data were calculated using the basic spherical Earth approximation. At 350 km altitude, the cross-track IFOV (ground swath) is 83 m (42.5 km) at nadir, rising to 115 m (57 km) at 30° and 182 m (93 km) at 45° . Because of this degradation of resolution, we anticipate that most of the HICO's observations will be done within 30° of nadir, but the HICO is a path-finding instrument and will be used to investigate the utility of larger off-nadir observations. The 45° observation angle, which translates to an off-zenith angle of 48° at the observed ground point, will allow us to investigate the accuracy with which atmospheric correction can be performed on hyperspectral data at this relatively large angle.

The along-track nadir IFOV is also 83 m. The sensor was calibrated and qualified for normal-mode operation at a frame time of 13.75 ms, which combines with the 7.0 km/s ground speed of the ISS to yield an along-track GSD of 96 m. In the along-track direction, the IFOV and GSD are different. Because of the increased range, the along-track IFOV increases to 95 m at 30° and to 120 m at 45° , but the GSD is set by the frame time and remains 96 m. In a standard scene, 2000 frames are taken, covering a length of 192 km, for a scene area at nadir of $42.5 \times 192 = 8200$ sq km. In HR mode, the frame time is 30 ms, GSD is 210 m, and 500 frames are taken for a scene length of 105 km.

The orientation of the HICO's footprint on the ground is determined by the latitude of the ISS when the observation is made. The orientation of the long

axis of a HICO scene with respect to due east is given in Fig. 9. The HREP carries a star tracker that gives precision attitude determination that can be combined with postprocessed ISS ephemeris data to calculate geolocations on a pixel-by-pixel basis. The accuracy of the star tracker is about 0.002° , a small fraction of a HICO pixel (0.014°).

4. Operations

The HICO executes a normal observation in the following way. Before the observation, the instrument is in stow position, with the lens looking into the labyrinth light seal (see Fig. 1). The seal is intended to establish the dark level for the sensor and to protect the lens, to the extent possible, from contaminants from the ISS. The observation begins by taking 200 frames of dark data. Data collection is stopped for 5 min while the motor turns the LOS to the desired direction for an Earth-surface observation. The stow position is 60° from the nadir direction. To make an observation at $+45^\circ$ off-nadir (to port or north), the bench needs to turn through only 15° , but it must turn through 90° to make an observation at -30° (to starboard or south). This motion takes place during the fixed 5 min interval. Camera data collection is reinitiated and 2000 frames are recorded. During a second 5 min pause, the bench returns to the stow position, after which another 200 frames of dark data are taken. Thus, the total data volume is 2400 frames with 512×128 samples per frame and two bytes per sample plus 256 header bytes (314,573,056 bytes, approximately equal to 315 MB). The entire process takes about 18 min. The transfer rate to the ISS is 1.5 Mbps, requiring another 28 min.

In HR mode, 100 frames of dark data are taken before and after the scene and 500 frames for the scene at a frame time of 30.05 ms. Each frame contains 384 spectral pixels, for a total data volume of 275 MB.

Mission planning takes place at the NRL. As described above, mechanical constraints limit us to one observation every 20 min or so, and obtaining hyperspectral images with a high SNR requires that the Sun be well above the horizon, so we are limited in practice to one scene per orbit. As previously noted, there are 15.7 orbits per day. Pointing and other commands for two to three days of operation are sent from NRL to the Payload Operations Integration Center (POIC) at the NASA Marshall Space Flight Center. This command script is normally updated every Monday, Wednesday, and Friday. From the POIC the commands are sent to the ISS and passed to the HREP's computer, which then autonomously issues commands to the HICO's camera and rotator. The image and ancillary data, e.g., from the star tracker, are stored in the HREP data system until transfer to the ISS to be downlinked by NASA. After reception on the ground, the data are sent from NASA to NRL for processing, analysis, distribution, and archiving.



Fig. 10. (Color online) HICO image of the South China Sea, near Hong Kong, China, taken on 2 October 2009. The ISS is moving north, and the orientation is from the SW at the bottom to the NE at the top.

5. Some Images and Early Experience

Red-green-blue excerpts from two of the HICO's early images are shown in Figs. 10 and 11. A few representative spectra from points in Fig. 11 are shown in Fig. 12.

As mentioned in the Introduction, previous experience has shown [2] that an SNR of 200 or better over the 400–700 nm waveband is required to derive en-

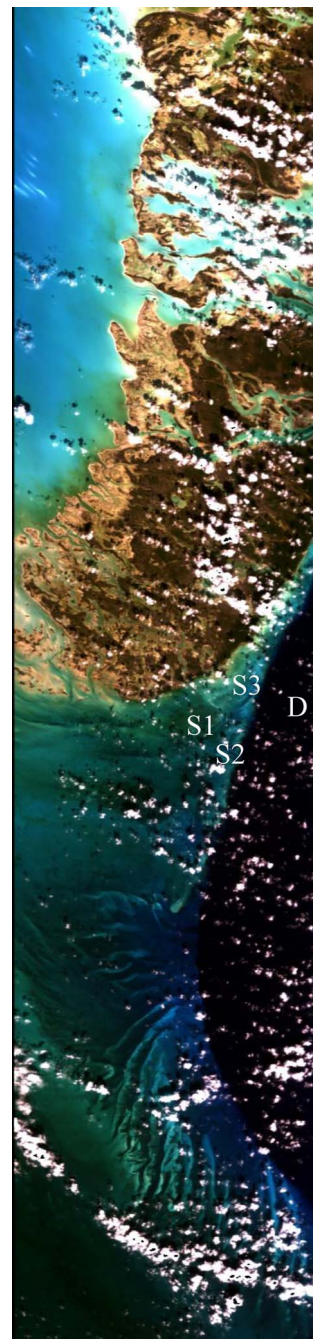


Fig. 11. (Color online) HICO image of Andros Island in the Bahamas, 22 October 2009, from the NW at the top to the SE at the bottom. Seafloor structures are visible in shallow water.

vironmentally relevant quantities from hyperspectral data. This information is derived from light that is scattered or reflected to the sensor from beneath the water surface. Figure 13 shows some HICO SNRs, obtained from the photon-limited formula of Subsection 2.E, from optically deep and shallow water, taken from the points indicated in Fig. 11. In this context, shallow (deep) water means that the bottom is (is not) visible. In Fig. 13, the normal 5.7 nm spectral samples have been binned by two to give 11.4 nm samples. For all samples, Rayleigh and

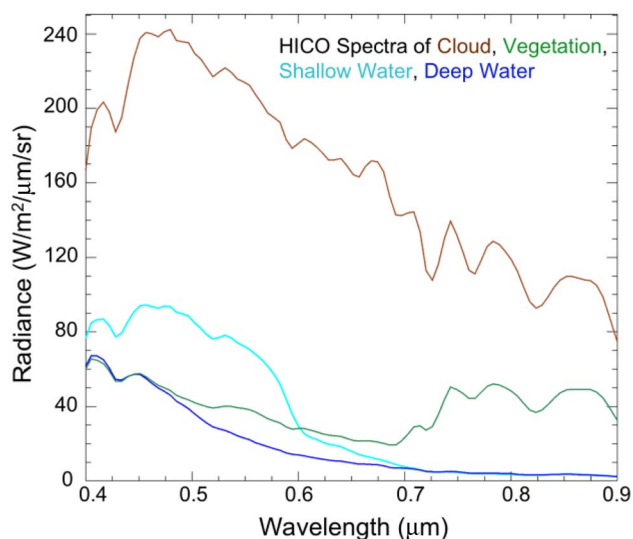


Fig. 12. (Color online) Representative spectra of points D, S1, S2, and S3 from Fig. 11.

aerosol scattering from the atmosphere is a large part of the total signal. In the deep water, there is a strong signal from the water in the blue, but essentially all of the signal is from the atmosphere for wavelengths >720 nm. Shallow water yields a higher signal because of scattering and reflectance from the bottom. For all samples, the HICO's SNR exceeds 200 for the 400–600 nm wavelength range, which is the range that is most critical for ocean studies.

Detailed examination of the HICO's images shows that the instrument's focus remains sharp, but we do conclude that there was a lateral shift between the spectrometer and the camera of about $70\text{ }\mu\text{m}$ in the spatial direction and about $8\text{ }\mu\text{m}$ in the spectral direction. The spectrometer and the camera are bolted to the optical bench but not directly to each other. Presumably, launch stresses caused a slight shift in their relative positions. The spatial shift caused the image of the spectrometer's slit to move slightly along its

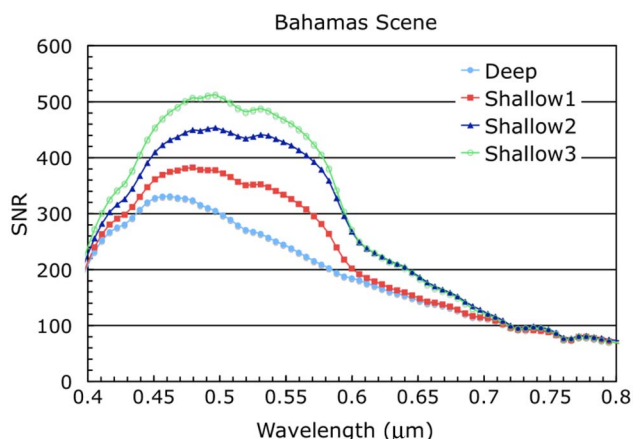


Fig. 13. (Color online) Representative SNR plots for HICO data from various water depths. D, S1, S2, and S3 refer to locations shown in Fig. 11. The normal 5.7 nm spectral samples have been binned by two to give 11.4 nm samples.

length, so that it no longer covers all 512 spatial pixels of the focal plane array. The result is a dark line at the right and left edges, respectively, of the images in Figs. 10 and 11. This line includes pixels 508–512, hence it appears on the starboard (south) side of the image, which, as displayed in Figs. 10 and 11, is on the right (left) when the ISS is moving north (south).

Analysis of HR images has shown an on-orbit wavelength shift from the laboratory calibration that has changed from 1.7 immediately after launch to 0.9 nm as of June 2010. This difference appears in the comparison between the actual location of known atmospheric (oxygen A band at 761 nm) and solar Fraunhofer lines (at 430 , 486 , 517 , and 656 nm) [19] in the HICO spectra and the locations predicted from laboratory measurements. We attribute the original wavelength shift of 1.7 nm to a mechanical alignment change at launch. Its magnitude was $(1.7\text{ nm})/(1.9\text{ nm per pixel}) \approx 0.9\text{ pixels} \approx 14\text{ }\mu\text{m}$. We do not know why the shift has changed; its present size is $0.9/1.9 \approx 0.5\text{ pixels} = 8\text{ }\mu\text{m}$, and it has not changed since June 2010.

We return to the spatial shift. As noted in Subsection 2.C, the accuracy with which the optic axis of the lens was determined to be aligned with the center of the CCD is about 2 pixels. Because we do not know whether the shift of about 4.5 pixels adds to or subtracts from this error, we have left Eq. (1) unchanged. The maximum possible effect is to change the third-order correction factor at the edge of the field by a negligibly small amount ($<0.002^\circ$).

Among the first images taken was a dark "image" on the night side of the Earth, with the lens not looking through the slit. Thus, there was no light on the CCD, and we were able to verify that the dark correction described in Appendix A works as well on orbit as on the ground. Also, by comparing the before-and-after dark frames (the first and last 200 of the 2400 total frames; see Section 4 and Appendix A) from the night side with those from a daylight observation, we were able to verify that the light from earthshine coming through the observation slit does not leak through the labyrinth seal into the lens and onto the CCD.

The HICO's biggest problem on orbit is with single-event upsets affecting the HREP's computer, which is a PC 104 running the Windows operating system. The computer locks up and must be restarted about once every three days of operation. Discussions with NASA personnel indicate that this is typical performance for PCs, of which there are many on the ISS. The downtime resulting from these lockups causes the HICO to miss, on average, about one in five of its planned scenes.

6. Discussion and Conclusion

The first primary goal of the HICO program was to build a space instrument that would meet the specifications for coastal ocean imaging, deliver it in less than 18 months, and have it operate for at least one

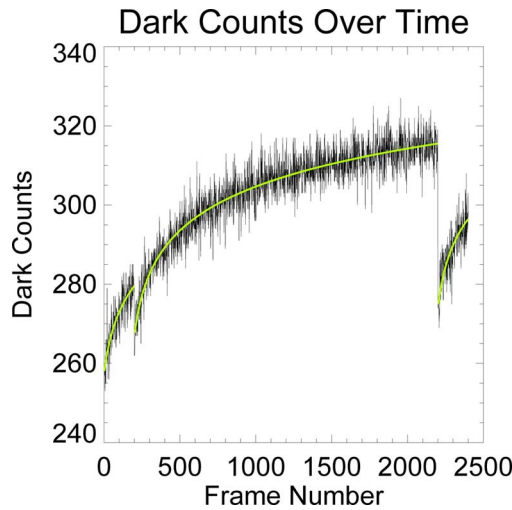


Fig. 14. (Color online) Data from a typical pixel are shown in black with the fitted curves from Eq. (A1) in white (see text). The first and last sets of 200 frames are dark data; the central 2000 frames are from the scene, also dark in this case. There is a 5 min break in data collection after the 200th frame and after the 2200th frame. Different datasets can have substantially different dark counts, as shown in Fig. 15.

year on the ISS. That has been accomplished, and over 1700 scenes were collected in the first year of operation.

Space-based instruments are often calibrated, tested, and recalibrated for a year or more before launch to assure they will operate and remain stable in space. The HICO program's schedule did not permit this. Furthermore, the calibration of ocean color sensors and other Earth-viewing sensors is generally checked with an on-board calibrator or by imaging the Moon [20]. The HICO program's cost and schedule did not permit the former, and the HICO cannot image the Moon from the ISS. Instead, again as with other Earth-viewing-sensors, on-orbit calibration is done by analysis of data taken coincidentally with other well-calibrated sensors, such as MODIS and MERIS, and by imaging well-characterized land and ocean calibration sites. The on-orbit calibration of the HICO will be described in a future publication.

The second primary goal of the HICO program is to produce and interpret hyperspectral data to provide a valuable new view of the coastal ocean. Oceanographic studies using HICO data are underway and will be reported in future publications.

Appendix A: Dark Count Subtraction

Figures 14 and 15 show examples of the dark counts in HICO data taken during the spacecraft's thermal vacuum test. As described in Section 4 for our normal mode of operation, the camera first takes 200 frames (2.75 s) of dark data, warming up as it does so. During this time, the dark count rate rises. There is a 5 min pause between the first dark dataset and the scene dataset; this is the time allotted for the sensor to move from the stow position to the position at which it will observe the scene. During this time, the CCD cools down, and it restarts at a different tem-

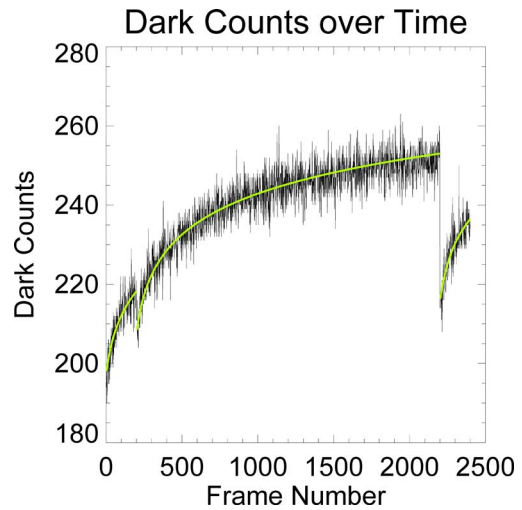


Fig. 15. (Color online) Same as Fig. 14, with a different dataset and different ambient temperature.

perature. It then rewarms for the 27.5 s of the scene (2000 frames) and cools off again in the 5 min pause before the second dark set (200 frames again), during which time the sensor returns to the stow position. To dark-correct the data, it is necessary (i) to find the functional form of the rise and (ii) to use the dark frames taken in the stow position to predict and subtract out the dark counts in the scene data. This will be done for normal mode operation, but not for the HR mode, because we have data only for the former.

In anticipation of Appendix B on frame smear correction, we note that this correction is not applied to the dark data. The reason is that the dark counts do not vary sufficiently from pixel to pixel to warrant such correction, as the results below will show. These results were obtained using HICO data generated during thermal vacuum testing, exactly as they will be generated on orbit.

Let $M(n)$, $0 \leq n \leq 2,399$, be the measured set of 2400 samples (in DN counts) from one pixel. (In this discussion, the term "pixel" actually refers to the three spectral pixels that are summed on the chip at readout in normal mode operation.) The three segments of the dataset are $0 \leq n \leq 199$, $200 \leq n \leq 2,199$, and $2,200 \leq n \leq 2,399$. The first two samples in each of the three segments are not valid data, because the charge well of the pixel needs to be cleared out; this is shown by the spikes in frames 200 and 2200 in Figs. 14 and 15. Consequently, the first three samples are not used. A time parameter, t , is started at zero for the valid data in each segment, so the datasets used and the corresponding time parameters are $3 \leq n \leq 199$ ($0 \leq t \leq 196$, i.e., $t = n - 3$), $203 \leq n \leq 2199$ ($0 \leq t \leq 1996$, i.e., $t = n - 203$), and $2203 \leq n \leq 2399$ ($0 \leq t \leq 196$, i.e., $t = n - 2203$).

The dark counts as a function of the time parameter for a particular pixel and dataset are described by the empirical expression

$$D_{pk}(t) = A_{pk} + B_p \ln\left(1 + \frac{t}{t_s}\right), \quad (\text{A1})$$

where D_{pk} is dark counts for pixel p in segment k , $k = 1 - 3$, A_{pk} and B_p are constants for the pixel, t = time measured in frame numbers (defined above), and $t_s = 41$ is the scale time for the logarithmic function. Figures 14 and 15 show examples of HICO data fitted with curves of the form given by Eq. (A1).

The parameters A_{pk} and B_p vary from one scene to the next, presumably because the CCD has different initial temperatures. A_{pk} can change by 60 counts or more between scenes, while B_p varies over a fairly narrow range, generally from about 11.4 to about 12.3 for the temperature range thus far analyzed. The pixel-to-pixel variation within a scene is generally only about 10–20 counts for A_{pk} and about 0.2–0.3 for B_p .

For the dark datasets ($k = 1, 3$), t has heretofore been a discrete variable labeling 197 samples of a pixel's output. In Eq. (A2) it is a continuous variable covering the interval $0 \leq t \leq t_m = 197$. The average of the function $f(t) = \ln(1 + t/t_s)$ over this interval is

$$\begin{aligned} f_{\text{ave}} &= \frac{t_s}{t_m} \int_0^{t_m} \ln\left(1 + \frac{t}{t_s}\right) \frac{dt}{t_s} \\ &= \frac{t_s}{t_m} \left[\left(1 + \frac{t}{t_s}\right) \ln\left(1 + \frac{t}{t_s}\right) - \left(1 + \frac{t}{t_s}\right) \right]_0^{t_m} \\ &= \frac{t_s}{t_m} \left[\left(1 + \frac{t_m}{t_s}\right) \ln\left(1 + \frac{t_m}{t_s}\right) - \left(1 + \frac{t_m}{t_s}\right) + 1 \right] \\ &= \left(1 + \frac{t_s}{t_m}\right) \ln\left(1 + \frac{t_m}{t_s}\right) - 1 = 1.125, \end{aligned} \quad (\text{A2})$$

where $t_s = 41$, $t_m = 197$ for the numerical value.

The average numbers of counts in the dark sets are given by the sums

$$S_1 = \frac{1}{197} \sum_{n=3}^{199} M(n) \quad \text{and} \quad S_3 = \frac{1}{197} \sum_{n=2203}^{2399} M(n). \quad (\text{A3})$$

We now define

$$S_{\text{ave}} = \frac{1}{2} (S_1 + S_3). \quad (\text{A4})$$

Data analysis has given the empirical relation

$$B_p = 11.4 + 0.9 \times \frac{S_{\text{ave}} - 221}{285 - 221}. \quad (\text{A5})$$

Now, from Eqs. (A1) and (A2) with $k = 1, 2$, we see that

$$\begin{aligned} \text{Ave}[D_{p1,3}(t), 0 \leq t \leq 197] &= A_{p1,3} + B_p f_{\text{ave}} \\ &= A_{p1,3} + 1.125 B_p. \end{aligned} \quad (\text{A6})$$

We now set Eq. (A6) equal to $S_{1,3}$ from Eq. (A3) to see that the fit parameters $A_{p1,3}$ are obtained from the data via

$$A_{p1,3} = S_{1,3} - 1.125 B_p. \quad (\text{A7})$$

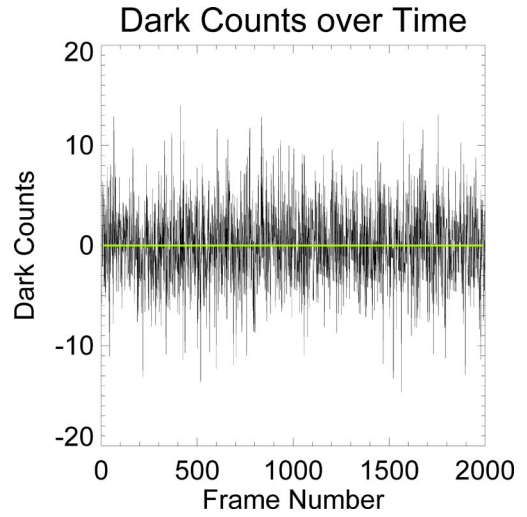


Fig. 16. Typical dark scene test data from one pixel with dark counts subtracted.

Data analysis has also shown that

$$A_{p2} = \frac{1}{2} (A_{p1} + A_{p3}) + 1.2. \quad (\text{A8})$$

Equation (A8) relates a prediction (right side) to an actual value (left side). Finally, the corrected data for the scene are given by

$$\begin{aligned} M_{\text{new}}(203 \leq n \leq 2199) &= M_{\text{old}} - \left[A_{p2} + B_p \right. \\ &\quad \left. \times \ln\left(1 + \frac{n - 203}{t_s}\right) \right]. \end{aligned} \quad (\text{A9})$$

In order to eliminate out-of-range values, the first three samples are deleted, so the processed data contain 1997 samples.

An example of a pixel output with dark counts subtracted is shown in Fig. 16. The histogram of the postsubtraction averages for a whole scene of dark

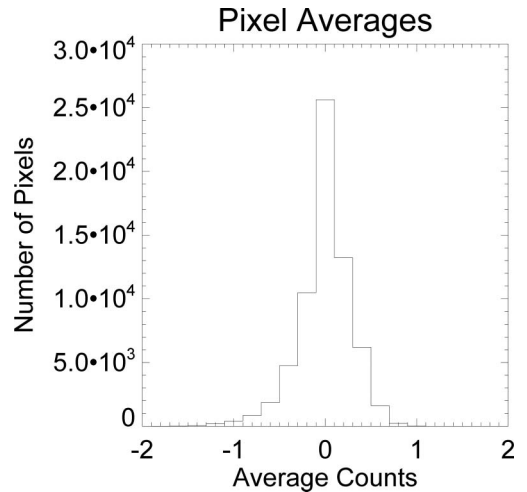


Fig. 17. Histogram of averages of corrected data for one dataset. The average of the pixel averages (the centroid of the histogram) is -0.005 .

data is shown in Fig. 17. The results presented here are good: the results presented in Figs. 16 and 17 show that dark count subtraction errors rarely exceed one full count. (The random dark noise level apparent in Fig. 16 has an rms value of about 3.8 counts.)

Appendix B: Frame Smear Correction

In the HICO, the frame transfer is done in the spectral direction. The “blue” pixels (pixels that receive blue light) are closest to the covered frame and enter it first, the “red” pixels last. During the transfer, the charge packet that will reside in the bluest pixel during the next exposure time passes through all the other pixels in its column and collects a charge from the light falling on these pixels. The reddest pixel collects no light before the stable exposure time starts. Intermediate pixels collect a charge from those pixels through which they pass. After the stable exposure time, the bluest pixel is immediately transferred into the covered frame and collects no more charge. The reddest pixel passes through all the other pixels in its column and collects a charge from them. Thus the bluest pixel receives light from before the exposure time, the reddest pixel from after, with intervening pixels receiving light from, proportionately, before and after. This problem can be fixed with data processing. The following development will focus on our normal bin-by-three mode of operation, but the same technique is applied to HR data simply by omitting the summing by three in the equations described below.

To exhibit a data-processing solution to the frame smear problem, we will first solve it for the case in which all 512 pixels in each column are recorded and under the assumption that the rate at which pixels receive charge during the transfer, either before or after the stable exposure time, is the same as during the stable exposure time. We will then extend the solution to the case in which pixels are binned at readout, not all are recorded, and information from the preceding and following exposures is used.

We denote by R_n , $1 \leq n \leq N = 512$, the count rate in (spectral) pixel n . During readout time T_2 (1.11 ms), there are 512 ticks of the frame-transfer clock, which divide the interval T_2 into $N - 1 = 511$ intervals of length $\delta T = (1.11 \text{ ms})/511 = 2.17 \mu\text{s}$. Thus $T_2 = (N - 1)\delta T$, and we note for use below that $T_2 + \delta T = N\delta T$. As a charge packet passes through pixel n , it spends time δT receiving counts at the rate R_n . The total measured counts (after dark count correction, discussed above) in pixel m are therefore

$$\begin{aligned} M_m &= R_m T_1 + \sum_{\substack{n=1 \\ n \neq m}}^N R_n \delta T \\ &= R_m (T_1 - \delta T) + \delta T \sum_{n=1}^N R_n. \end{aligned} \quad (\text{B1})$$

The desired quantity is the corrected count C_m that would be in the pixel after the full exposure time if the smear effect were not present:

$$C_m = (T_1 + T_2)R_m. \quad (\text{B2})$$

We now substitute Eq. (B2) into Eq. (B1) to find

$$M_m = \frac{C_m}{T_1 + T_2} (T_1 - \delta T) + \frac{\delta T}{T_1 + T_2} \sum_{n=1}^N C_n, \quad (\text{B3})$$

and we observe that

$$\begin{aligned} \sum_{m=1}^N M_m &= \frac{T_1 - \delta T}{T_1 + T_2} \sum_{m=1}^N C_m + N \frac{\delta T}{T_1 + T_2} \sum_{n=1}^N C_n \\ &= \frac{T_1 + (N - 1)\delta T}{T_1 + T_2} \sum_{m=1}^N C_m = \sum_{m=1}^N C_m, \end{aligned} \quad (\text{B4})$$

where $T_2 = (N - 1)\delta T$ has been used. Equation (B4) says that counts are conserved. We now rearrange Eq. (B3) to obtain

$$\begin{aligned} C_m &= \frac{T_1 + T_2}{T_1 - \delta T} M_m - \frac{\delta T}{T_1 - \delta T} \sum_{n=1}^N C_n \\ &= M_m + \frac{T_2 + \delta T}{T_1 - \delta T} \left(M_m - \frac{1}{N} \sum_{n=1}^N C_n \right), \end{aligned} \quad (\text{B5})$$

where $T_2 + \delta T = N\delta T$ has been used, and substitute from Eq. (B4) into Eq. (B5) to find

$$C_m = M_m + \frac{T_2 + \delta T}{T_1 - \delta T} \left(M_m - \frac{1}{N} \sum_{n=1}^N M_n \right). \quad (\text{B6})$$

We observe that the correction applied to M_m to obtain C_m is positive if M_m is greater than the average of the M_n and negative if it is less.

Equation (B6) can be adapted to the case of our normal bin-by-three mode by the simple expedient of adding sets of three equations together. This reduces 512 pixels to 171 bins ($3 \times 171 = 512 + 1$), so bin 171 contains only 2 pixels), of which 128 are recorded. Bins 129–171 have a spectral range of 1080–1325 nm. The CCD detector, being made of silicon, is not sensitive to light beyond about 1100 nm, so the detected illumination in the unrecorded pixels comes almost exclusively from second- and third-order diffraction from the grating with, perhaps, a small contribution from scattered light. These counts can therefore be estimated from the data itself, but at present they are estimated simply by assuming $M_{m>128} = M_{128}$. Because there are very few counts in these channels, an error in estimating them does not have a serious effect. Equation (B6) becomes

$$C_m = M_m + \frac{T_2 + \delta T}{T_1 - \delta T} \left(M_m - \frac{3}{512} \sum_{n=1}^{171} M_n \right), \quad (\text{B7})$$

where C_m and M_m are redefined to be sums of three pixels; the indices run from 1 to 171, instead of from 1 to 512, and $T_1 = 12.64$ ms, $T_2 = 1.11$ ms, $\delta T = 2.17$ μ s. Equation (B7) is our method for correcting HICO data for frame smear effects.

The HICO was built by the NRL as a fast-response program to seize a flight opportunity on the ISS. This rapid response was made possible by the Innovative Naval Prototype (INP) program sponsored by the Office of Naval Research. The HICO was integrated and flown under the direction of the Department of Defense's Space Test Program. We gratefully acknowledge support from National Aeronautics and Space Administration (NASA) and the Japan Aerospace Exploration Agency for the launch and support of the HREP on the ISS. We thank Bo-Cai Gao for analyzing the on-orbit wavelength calibration data.

References

1. C. O. Davis, J. Bowles, R. A. Leathers, D. Korwan, T. V. Downes, W. A. Snyder, W. J. Rhea, W. Chen, J. Fisher, W. P. Bissett, and R. A. Reisse, "Ocean PHILLS hyperspectral imager: design, characterization, and calibration," *Opt. Express* **10**, 210–221 (2002).
2. C. O. Davis, K. L. Carder, B.-C. Gao, Z. P. Lee, and W. P. Bissett, "The development of imaging spectrometry of the coastal ocean," in *Proceedings of the IEEE Conference on International Geoscience and Remote Sensing Symposium* (IEEE, 2006), Vol. 4, pp. 1982–1985.
3. C. O. Davis, M. Kavanaugh, R. Letelier, W. P. Bissett, and D. Kohler, "Spatial and spectral resolution considerations for imaging coastal waters," *Proc. SPIE* **6680**, 66800P (2007).
4. Z. P. Lee and K. L. Carder, "Effects of spectral-band number on retrievals of water column and bottom properties from ocean-color data," *Appl. Opt.* **41**, 2191–2201 (2002).
5. S. A. Budzien, R. L. Bishop, A. W. Stephan, P. R. Straus, A. B. Christensen, and J. H. Hecht, "The remote atmospheric and ionospheric detection system on the ISS: mission overview," *Proc. SPIE* **7438**, 74380X (2009).
6. A. W. Stephan, S. A. Budzien, R. L. Bishop, P. R. Straus, A. B. Christensen, J. H. Hecht, and Z. Van Epps, "The remote atmospheric and ionospheric detection system on the ISS: sensor performance and space weather applications from the extreme to the near ultraviolet," *Proc. SPIE* **7438**, 74380Y (2009).
7. R. L. Bishop, S. A. Budzien, J. H. Hecht, A. W. Stephan, A. B. Christensen, P. R. Straus, and Z. Van Epps, "The remote atmospheric and ionospheric detection system on the ISS: sensor performance and space weather applications from the visible to the near infrared," *Proc. SPIE* **7438**, 74380Z (2009).
8. D. R. Korwan, R. L. Lucke, M. Corson, J. H. Bowles, B. G. Gao, R. R. Li, M. J. Montes, W. A. Snyder, N. R. McGlothlin, S. D. Butcher, D. L. Wood, C. O. Davis, and W. D. Miller, "The Hyperspectral Imager for the Coastal Ocean (HICO)—design and early results," in *IGRSS Workshop on Hyperspectral Image and Signal Processing: Evolution in Remote Sensing* (IEEE, 2010), pp. 14–16.
9. D. R. Korwan, R. L. Lucke, N. R. McGlothlin, S. D. Butcher, D. L. Wood, J. H. Bowles, M. Corson, W. A. Snyder, C. O. Davis, and D. T. Chen, "Laboratory characterization of the Hyperspectral Imager for the Coastal Ocean (HICO)," in *Proceedings of the IEEE Conference on Geoscience and Remote Sensing Symposium* (IEEE, 2009), Vol. 2, pp. II-69–II-72.
10. M. Corson, R. L. Lucke, and C. O. Davis, "The Hyperspectral Imager for the Coastal Ocean (HICO) and environmental characterization of the coastal zone from the International Space Station," in *Optical Remote Sensing of the Environment*, OSA Technical Digest (CD) (Optical Society of America, 2010), paper OMA4.
11. M. R. Corson, R. L. Lucke, J. H. Bowles, D. Chen, B.-C. Gao, D. R. Korwan, R.-R. Li, W. A. Snyder, C. O. Davis, and W. D. Miller, "The Hyperspectral Imager for the Coastal Ocean (HICO) environmental littoral imaging from the International Space Station," in *Proceedings of the 2010 IEEE International Geoscience and Remote Sensing Symposium* (IEEE, 2010), pp. 3752–3755.
12. P. Mouroulis, R. O. Green, and T. G. Chrien, "Design of pushbroom imaging spectrometers for optimum recovery of spectroscopic and spatial information," *Appl. Opt.* **39**, 2210–2220 (2000).
13. R.-R. Li, R. Lucke, M. Corson, D. Korwan, and B.-C. Gao, "Correction of second order light for the HICO™ sensor on board the International Space Station," in *Proceedings of the 2010 IEEE International Geoscience and Remote Sensing Symposium* (IEEE, 2010), pp. 2303–2306.
14. H. R. Gordon, T. Du, and T. Zhang, "Atmospheric correction of ocean color sensors: analysis of the effects of residual instrument polarization sensitivity," *Appl. Opt.* **36**, 6938–6948 (1997).
15. G. Meister, E. J. Kwiatkowska, B. A. Franz, F. S. Patt, G. C. Feldman, C. R. McClain, "Moderate resolution imaging spectrometer ocean color polarization correction," *Appl. Opt.* **44**, 5524–5535 (2005).
16. ZEMAX Development Corporation, Bellevue, Washington 98004, USA.
17. <http://www.spaceref.com/news/viewsr.rss.html?pid=35180>.
18. <http://news.bbc.co.uk/2/hi/science/nature/8141256.stm>.
19. B.-C. Gao, M. J. Montes, and C. O. Davis, "Refinement of wavelength calibrations of hyperspectral imaging data using a spectrum-matching technique," *Remote Sens. Environ.* **90**, 424–433 (2004).
20. R. A. Barnes, R. E. Eplee, F. S. Patt, and C. R. McClain, "Changes in the radiometric sensitivity of SeaWiFS determined from lunar and solar-based measurements," *Appl. Opt.* **38**, 4649–4664 (1999).